Failure Mode Analysis and a Mechanism for Hot-Ductility Improvement in the Nb-Microalloyed Steel

FARAMARZ ZARANDI and STEVE YUE

Loss of hot ductility at the straightening stage of the continuous casting of high-strength low-alloy steel is attributed to different microalloying elements, in particular, Nb. However, such elements are essential for the desired mechanical characteristics of the final product. Since the chemistry cannot be altered to alleviate the problem, thermomechanical processing was studied in order to improve the hot ductility. Two Nb-microalloyed steels, one also containing B, were examined. The thermal history occurring in the continuous casting process was taken into account as well. First, it was noticed that the steel with B has a higher hot ductility than the other after being subjected to *in-situ* melting followed by the thermal schedule. Grain boundary sliding was recognized as the failure mechanism. Then, the effect of deformation applied in the vicinity of the $\delta \rightarrow \gamma$ transformation, while the thermal schedule was being executed, was investigated. Such deformation appeared to improve the hot ductility remarkably. Finally, the mechanism of such improvement in the hot ductility was elaborated.

I. INTRODUCTION

CONTINUOUSLY cast steel, whether cast in a curved or straight and vertical mold, eventually has to be straightened horizontally when it has solidified throughout its cross section. During this straightening operation, a tensile strain of about 1 to 2 pct at a strain rate between 10^{-3} and 10^{-4} s^{-1} can be generated on the top surface of a slab/billet.[1] Loss of hot ductility during the straightening operation, where the surface temperature can vary from 700 °C to 1200 °C, has been a serious problem in carbon and low alloy steels since it is associated with transverse surface cracking. Even though extensive work has been done to resolve this problem, hot cracking still persists. The process of crack removal (scarfing) interferes with productivity, and cracks can even lead to scrapping of a coil. In addition, a current trend in steel processing technology is to integrate the rolling process with the continuous casting process through "direct rolling" (rolling of hot slabs without reheating) or "hot charging" (charging of hot slabs into the reheating furnace). This does not allow for any tolerance of surface cracks, since there is no interruption between casting and subsequent hot rolling processes for inspection and scarfing.

Generally, the mechanisms of the hot ductility loss in steel have been attributed to the grain boundary, or the region adjacent to the grain boundary, which can be weaker than the grain interior.[1–7] This leads to strain concentrations at or near the grain boundary and, consequently, grain boundary decohesion. Through numerous investigations, it has been found that the thermal history and alloying/residual elements play roles in this respect.[1,8–10] Therefore, some solutions based on these findings have been proposed and applied. Addition of Mn will scavenge sulfur and prevent its segregation to grain boundaries; hence, grain boundary weakness is reduced in the C-Mn steel. Also, B has been found to improve the hot ductility in the Nb-containing steel, probably by altering segregation patterns and strengthening grain boundaries.[11] Nevertheless, the problem is much more complicated in the microalloyed steels and to date there has been no specific and applicable solution. This can be attributed to the fact that most investigations have been centered on the alloying elements. For instance, in the Nb-containing steel, Nb has been identified to cause the loss of hot ductility, but removing or scavenging Nb from the lattice would come at the expense of the mechanical properties that are characteristic of high-strength low-alloy steels. Addition of B may not always be practical since it scavenges N and so reduces the amount of N available for carbonitride precipitation, which is essential in developing the mechanical properties.[12] Also, B encourages ferrite formation inside grains.[13] Moreover, the nonequilibrium co-segregation of B and Nb retards dynamic recrystallization,[14,15] which can also influence the mechanical characteristics. On the other hand, these laboratory findings were obtained on the specimens reheated to high temperatures, but not melted, and then cooled to the test temperatures. Hence, they may not be fully applicable to the continuous casting process, which involves melting, solidification, and segregation of alloying elements. Specimens for the hot ductility test are usually made from steel plates that are hot worked and therefore homogenized. However, melting specimens *in situ*, before evaluating the hot ductility, ensures resolution of precipitates such as TiN and MnS,[10] as well as the generation of the inhomogeneities typical of an as-cast structure.

Finding a solution to transverse cracking without altering the steel chemistry is always a preferred approach. The approach of this work is to consider high-temperature deformation as a means to alleviate the problem of hot ductility in the Nb-containing steel. A Nb-microalloyed steel containing B was also chosen for comparison.

II. EXPERIMENTS

Two grades of microalloyed steels with chemistries shown in Table I were selected. They had been continuously cast and hot rolled down to 13-mm thickness. Cylindrical specimens

---

FARAMARZ ZARANDI, Research Associate, and STEVE YUE, Professor, are with the Department of Metals and Materials Engineering, McGill University, Montreal, PQ, Canada H3A 2B2. Contact e-mail: faramarz.zarandi@mail.mcgill.ca

Manuscript submitted April 2, 2004.

Table I. Steel Chemistries (Weight Percent)

Elements	C	Mn	P	S	Si	Nb	Ti	Al	Cr	Ni	Mo	Sn	Cu	B	N
B steel	0.015	1.65	0.009	0.008	0.23	0.05	0.02	0.02	<0.003	<0.003	<0.0017	<0.001	0.001	29 ppm	48 ppm
Nb steel	0.058	1.21	0.008	0.011	0.159	0.037	0.02	0.02	0.05	0.12	0.03	0.02	0.462	NA	78 ppm

with diameter of 9.5 mm and length of 125 mm were machined; because the specimens were subsequently melted, the orientation (with respect to the rolling direction) was not relevant. Specimens, 15 mm threaded in both ends, were vertically screwed into the upper and lower anvils of the deformation machine (MTS). The entire specimen length and part of the anvils were enclosed in a quartz tube. A protective atmosphere of argon containing 1 pct hydrogen was supplied inside the quartz tube to reduce oxidation of the iron on the specimen. An induction heating power supply was used to heat the specimen. The specimen temperature was measured, from outside the quartz tube, by a dual infrared radiation wavelength detector, which was not significantly affected by undersized objects that do not fill the field of view, bursts of steam, dust, etc. in the sight path. Also, helium was used to achieve high cooling rates where required by the thermal schedule.

Two different thermal schedules similar to those experienced by the billet surface in the continuous casting process, as shown in Figure 1,[16,17] were employed. The purpose of choosing the billet surface thermal history was to generate the billet surface microstructure since transverse cracking occurs on the surface. Also, specimens were melted *in situ* in order to dissolve all precipitates and sulfides and to simulate the large grain size and segregation developed during billet solidification. Due to a combination of liquid viscosity, liquid surface tension, and electromagnetic field, it was possible to hold the liquid by levitation for 5 to 10 seconds before solidification started. In this way, a melted gage length of 15 mm was obtained. Solidification began by applying the desired thermal schedule (Figure 1), and the hot ductility was isothermally evaluated at the straightening stage, as specified in Figure 1, by performing a tensile experiment to fracture at a rate of 5×10^{-3} s^{-1}. This strain rate is similar to the rate of straightening deformation in the continuous casting process.[1] Reduction in area (RA) after fracture quantified the hot ductility.

Thermal expansions and contractions of specimens during the thermal schedules were continuously and automatically compensated by the MTS anvil displacement so that the load on specimens was maintained around zero, except when there was a deformation.

First, the hot ductility at the straightening stage was studied in specimens that were solely subjected to the thermal schedules. Then, in order to study the effect of deformation on the hot ductility, specimens were deformed in compression during cooling after solidification, while the thermal schedule was proceeding; i.e., deformation was incorporated with the thermal schedule. Such deformations went continuously through different regions of δ-ferrite, $\delta \rightarrow \gamma$ (austenite) transformation, and austenite, as shown schematically in Figure 1. The strains and strain rates examined in this respect were $\varepsilon = 0.1$, 0.15 and $\dot{\varepsilon} = 0.003, 0.009, 0.027$ s^{-1}, respectively. In another set of experiments, $\varepsilon = 0.02$, 0.04, 0.06, 0.08, and 0.1 at $\dot{\varepsilon} = 0.003$ s^{-1} were applied to the Nb-steel specimens during cooling after solidification. All these deformations were initiated at the same temperature except $\varepsilon = 0.1$, which was initiated at a lower temperature. Throughout this article, these deformations will be referred to as predeformations. In all these experiments, the specimens were unloaded immediately after achieving the desired amount of precompression and were then subjected to the remaining portion of the thermal schedule, toward the straightening stage. Finally, the hot ductility was evaluated at the straightening stage, as described previously.

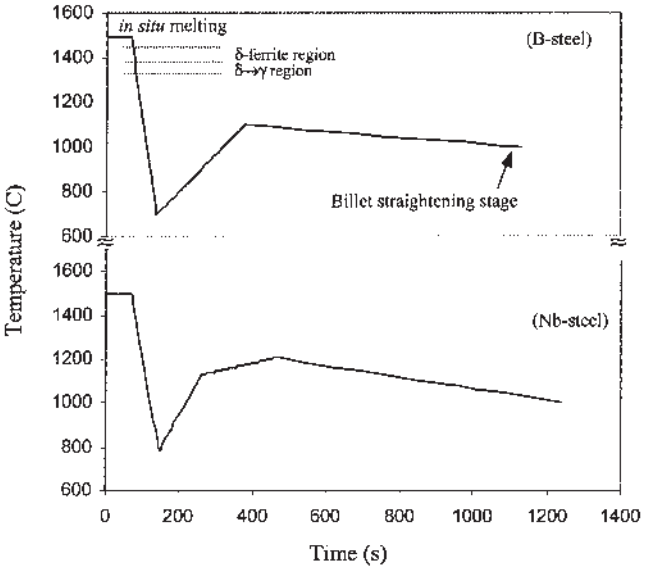

Fig. 1—Thermal schedules used to simulate the thermal condition occurring on the billet surface in the continuous casting process.[16,17]

The mechanism of failure was characterized in optical and the following electron microscopes: a JEOL*-840 scanning electron microscope and a Hitachi-4700 high-resolution field-emission SEM. Microstructures obtained by quenching specimens at the straightening stage of the thermal schedules were etched using either "picral" or a mixture of 80 mL water + 28 mL 10 pct aqueous oxalic acid in water + 4 mL 30 pct hydrogen peroxide. The final etchant is referred to as "X" throughout the article.

III. RESULTS

A. *Stress-Strain Behavior*

Figure 2 demonstrates that the steels experience a strength transition during cooling after the solidification. Obviously, the higher strengthening rate after the transition, which occurs at "a" and "b," cannot be solely explained by the decrease in temperature. Therefore, the effect of deformation rate in the proximity of the transition was studied. This, together with the subsequent tensile characteristics at the straighten-

---

*JEOL is a trademark of Japan Electron Optics Ltd., Tokyo.

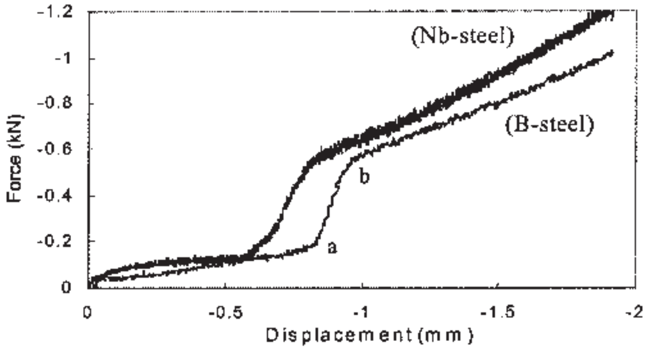

Fig. 2—Deformation behavior of the steels during cooling after solidification. Compression, incorporated with the thermal schedules, started at 1400 °C ($\dot{\varepsilon} = 3 \times 10^{-3}$ s^{-1} and $\dot{T} = 10$ °C/s).

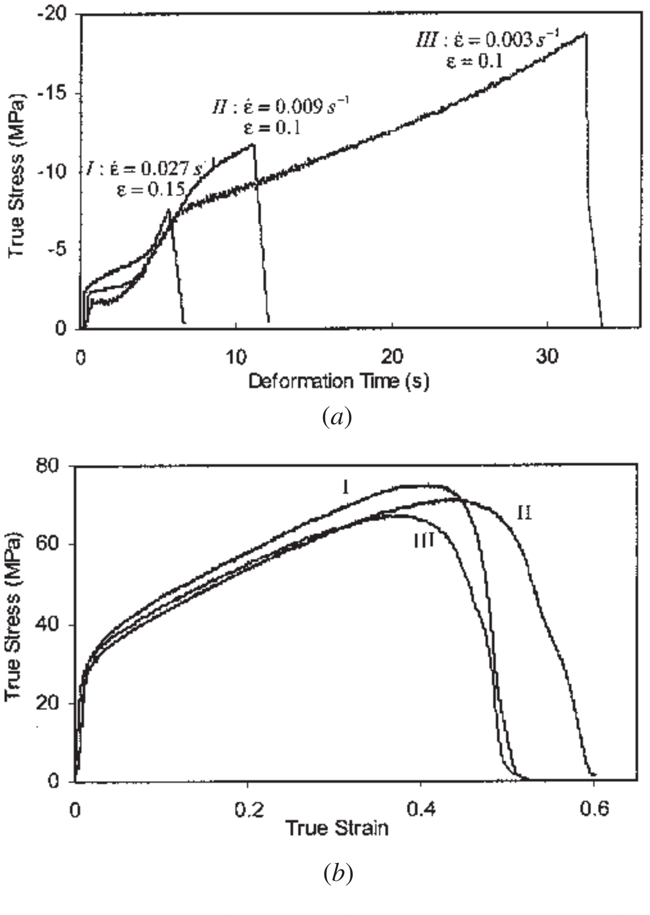

(*a*)

(*b*)

Fig. 3—(*a*) Application of various predeformation rates during cooling after solidification over the thermal schedule (all predeformations started at 1400 °C). (*b*) Respective tensile stress-strain curves at the straightening stage (Nb steel).

ing stage, is shown in Figure 3 for the Nb steel. As Figure 3(a) shows, the precompression terminated within the transition region for $\dot{\varepsilon} = 0.027$ s^{-1}, whereas it continued well after the transition region for $\dot{\varepsilon} = 0.003$ s^{-1}. Figure 3(b) demonstrates that precompression schedule II led to the highest elongation at the straightening stage. The higher strength in specimen I is attributed to a bulging effect, which occurred in the gage length due to the greater amount of precompression, *i.e.*, $\varepsilon = 0.15$ at $\dot{\varepsilon} = 0.027$ s^{-1}, executed at higher temperatures. (Note that the original diameter was used in the true stress calculation.) However, the effect of this on the RA evaluation is negligible.

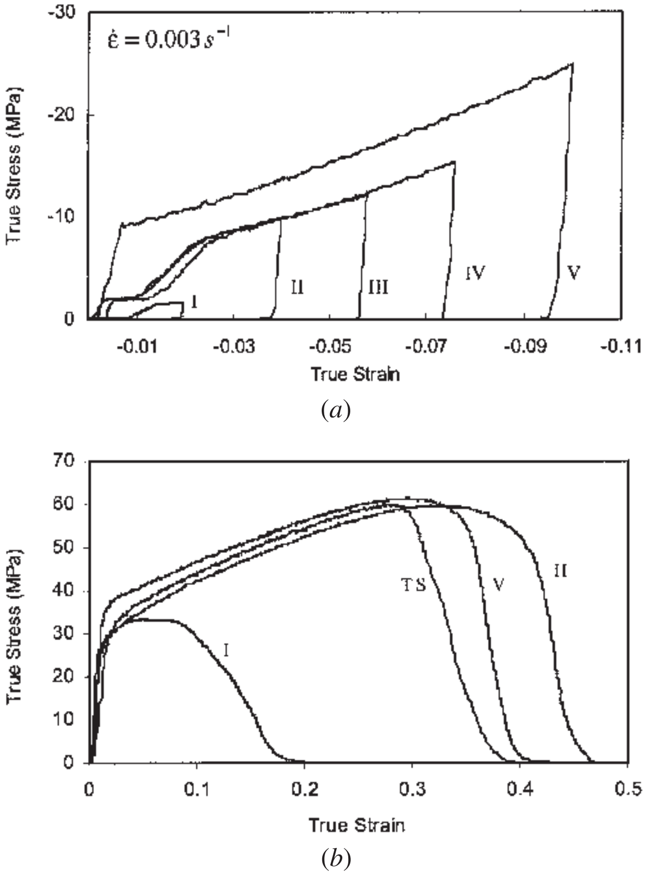

(*a*)

(*b*)

Fig. 4—(*a*) Various amounts of precompression that initiated before (I, II, III, IV) and after (V) the strength transition during cooling after solidification over the thermal schedule. (*b*) Stress-strain curves of respective specimens at the straightening stage. TS: thermal schedule alone (Nb steel).

Figure 4(a) shows the stress-strain curves for different amounts of precompression that were applied through the transition region. The precompression curves for $\varepsilon = 0.02$ and 0.1, which were respectively applied before and after the transition, are also included. The corresponding tensile stress-strain curves at the straightening stage are shown in Figure 4(b). The tensile deformation curve of the specimen subjected to the thermal schedule (TS) alone, *i.e.*, no predeformation, is also included for comparison. It is observed that predeformation before the transition is deleterious to the mechanical characteristics but beneficial if applied during or after the transition, comparing specimens I, II, and V with TS in Figure 4(b). Note that specimens III and IV, not presented in Figure 4(b), also exhibited a similar tensile behavior to that of specimen II.

However, the tensile characteristics of the B steel did not change markedly when there was a precompression before or during the transition, as compared to the effect of the thermal schedule alone. This is illustrated in Figure 5.

B. *Hot Ductility Evaluation*

The results of the hot ductility assessment at the straightening stage are summarized in Table II. Generally, applying

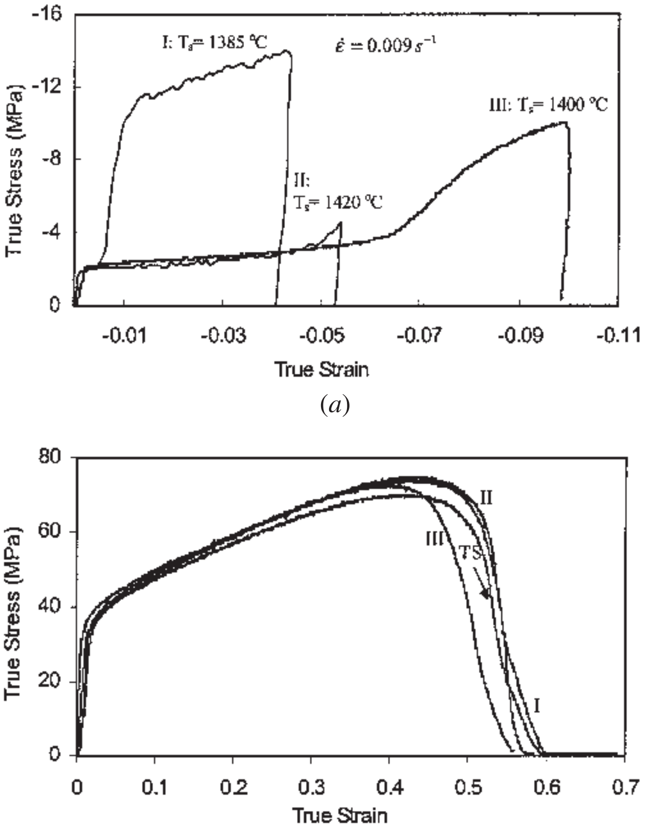

(*a*)

(*b*)

Fig. 5—(*a*) Precompression started at different temperatures (T_s) during cooling after solidification over the thermal schedule. (*b*) Respective stress-strain curves at the straightening stage. TS: thermal schedule alone (B steel).

Table II. Results of Hot Ductility Evaluation

Deformation Schedule	RA%
	B Steel
Thermal schedule alone	60
Fig. 5 (specimen I)	66
Fig. 5 (specimen II)	56
Fig. 5 (specimen III)	64
	Nb Steel
Thermal schedule alone	15
Fig. 4 (specimen I)	13
Fig. 4 (specimen II)	27
Fig. 4 (specimen III)	27
Fig. 4 (specimen IV)	28
Fig. 4 (specimen V)	23
Fig. 3 (specimen I)	42
Fig. 3 (specimen II)	53
Fig. 3 (specimen III)	41

predeformation before and during the transition alters the hot ductility within a narrow range in the B steel. This range of change is much wider in the Nb steel, which has a much lower intrinsic hot ductility when subjected to the thermal schedule alone. In both steels, the application of predeformation before the transition is somewhat harmful to the hot ductility, but beneficial when it is performed through the transition region. However, only the beneficial effect of predeformation is addressed in this article.

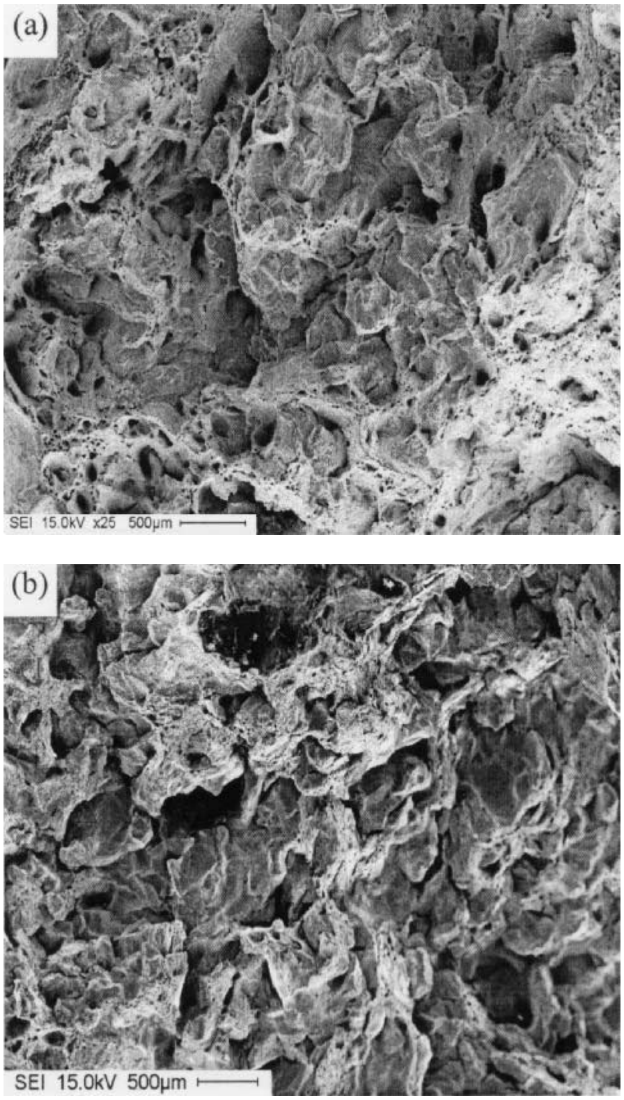

Fig. 6—Fracture surfaces of (*a*) the B steel and (*b*) the Nb steel at the straightening stage of the thermal schedules.

Even though the predeformation after the transition improved the hot ductility in the Nb steel, the highest hot ductility was achieved when such predeformation was preceded with a predeformation applied during the transition, comparing specimens V and III of Figures 4 and 3, respectively, in Table II. In other words, the effect of predeformation after the transition on the hot ductility improvement can be enhanced if it follows a predeformation applied during the transition. This can be clearly perceived by comparing the RA values of 28, 23, and 41 pct in Table II. Additionally, the predeformation rate appears to be influential. It is observed that there is an optimum combination of strain and strain rate, which leads to the highest hot ductility, *i.e.*, 53 pct RA.

C. *Fractography and Microstructures*

Fracture surfaces of both the B steel and the Nb steel after the thermal schedule alone (Figure 6) reveal both ductile and brittle (intergranular) characteristics. However, the intergranular mode is more prominent in the Nb steel. Examination of microstructures quenched immediately after fracture revealed that the failure was associated with grain boundary microcracks (Figure 7). The matrix is basically bainite with some martensite islands. Linkage of microcracks in some regions resulted in formation of macrocracks and grain boundary cavities. Moreover, it is observed that cracks have formed parallel to the tensile direction in the B steel, while they are almost normal to the tensile direction in the Nb steel. The grain boundary cavities are much larger in the Nb steel, and grain boundaries near the fracture edge are decorated with cracks/cavities that have grown or coalesced. This implies that microvoids linked together more easily in this steel. The grain size in the B steel varies from 10 to 150 μm near the fracture region (Figure 7(a)), whereas it is larger than 400 μm in the region far from the fracture edge. Obviously, the small grain sizes are not typical of an as-cast structure. The Nb steel, on the contrary, displays grain sizes ranging from 282 to 891 μm with an average $\sim$500 μm (Figure 7(b)).

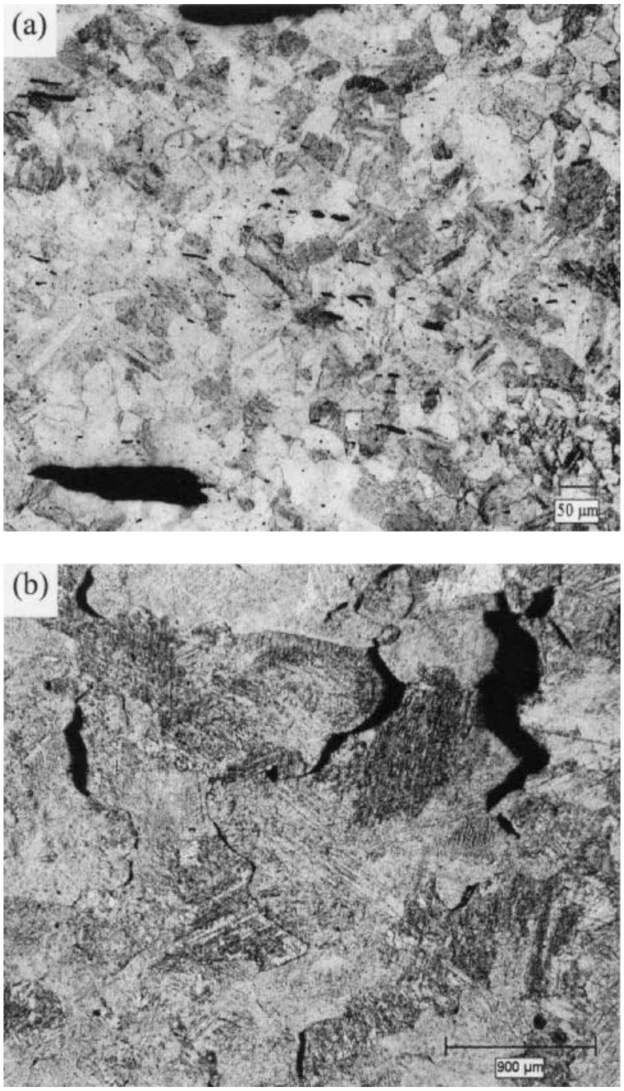

Fig. 7—Longitudinal microstructures of (*a*) the B steel and (*b*) the Nb steel quenched after fracture at the straightening stage (etched with X).

After application of predeformation during the transition, grain boundary cracking was suppressed to some extent. This can be deduced after comparing the microstructures in Figures 8(a) and 7(b), where Figure 8(a) displays a finer grain size as well. Fracture features were also finer. Figure 8(b) shows that the application of $\varepsilon = 0.1$ precompression during the transition refined the microstructure at the straightening stage, just before performing the tensile experiment. As can be seen, austenite grains are decorated with grain boundary ferrite and their average size is 220 μm. Such grain size is much smaller than that developed during the thermal schedule alone, *i.e.*, $\sim$500 μm or larger, which was also similar to the microstructure shown in Figure 7(b).

Similar microstructures and fracture features were observed in specimens I and III of Figure 3. In fact, the effect of predeformation rate during the transition (Figure 3(a)) on the grain size at the straightening stage could hardly be discriminated among specimens I through III. The important point

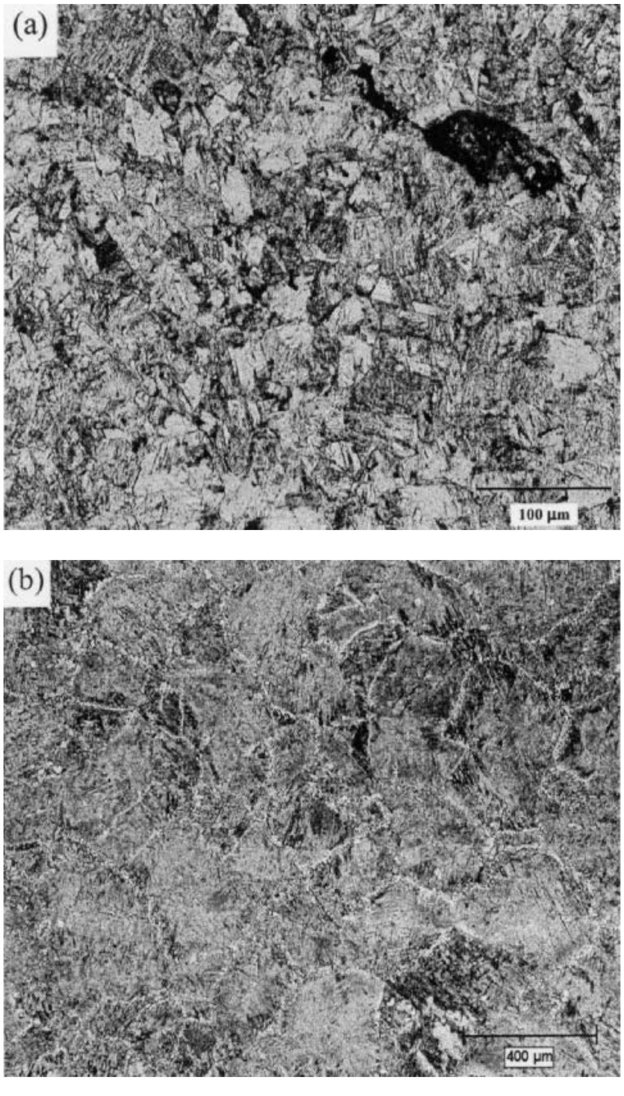

Fig. 8—(*a*) Longitudinal microstructure of specimen II in Fig. 3 quenched after fracture. (*b*) Longitudinal microstructure of a Nb-steel specimen subjected to a precompression schedule similar to that of specimen II in Fig. 3(a) and quenched just before performing the tensile test at the straightening stage (etched with X and picral, respectively).

is that grain boundary cavities are much smaller, isolated, and have oval shapes, instead of large, elongated, and linked-up cavities that resulted in propagation of cracks along grain boundaries, as shown in Figure 7(b). Oval cavities are also observed in grain interiors. A similar result was observed in the B steel fractured at the straightening stage after predeformation during the transition. However, such predeformation led to much less grain refinement after fracture in the B steel than the Nb steel, as compared with the grain sizes developed over the thermal schedules alone (Figure 7(a)).

It was also observed that all specimens I through V presented in Figure 4 fractured through grain boundary decohesion. In these specimens, cracks initiated mainly at grain boundary triple junctions and propagated along the boundaries, leading to complete separation of grains. However, the microstructures of specimens I and V, quenched after fracture at the straightening stage, displayed the largest average grain size, *i.e.*, ~500 μm, whereas specimens II through IV exhibited fairly identical average grain sizes, *i.e.*, ~350 μm.

IV. DISCUSSION

A. *The Strength Transition at Very High Temperature*

According to the iron-carbon equilibrium phase diagram, solidification of the steels examined here begins and completes with nucleation and growth of δ-ferrite dendrites, which subsequently transform to austenite. Hence, the strength transition during cooling after solidification (Figure 2) can be attributed to the $\delta \rightarrow \gamma$ transformation, which occurs within 30 °C. The stacking fault energy and the kinetics of dynamic recovery are lower in austenite than in δ-ferrite. Therefore, austenite is expected to appear stronger than δ-ferrite. On the other hand, with respect to the strain rate and temperature applied to the specimens in Figure 2, it can be reasonably assumed that the steels follow the power-law creep. Accordingly, the shear strength at very high temperatures, where the lattice diffusion is dominant, can be determined as follows:[18]

$$\sigma_s = \mu \left[\frac{\dot{\gamma} \mathrm{k} T}{A_2 \, D_v \mu \mathbf{b}} \right]^{\frac{1}{n}}$$

where μ is the shear modulus at temperature T, $\dot{\gamma}$ is the shear strain rate, k is the Boltzmann's constant, D_v is the lattice diffusion coefficient at temperature T, **b** is the Burgers vector, n is the exponent of the power-law creep, and A_2 is the Dorn constant. Regarding the temperature range and strain rate employed for the specimens in Figure 2 and typical values for the independent parameters in Reference 18, the shear stresses of austenite and δ-ferrite in the vicinity of 1380 °C are approximated as 11.31 and 4.06 MN/m^2, respectively. Hence, there would be a sudden increase in the strength when δ-ferrite transforms to austenite. This strength ratio is also consistent with the ratio of stresses at "b" and "a" in Figure 2.

The predeformation applied after solidification began in the single phase of δ-ferrite, which almost exhibits no strain hardening due to the fast kinetics of dynamic recovery. This is represented by the plateau segment of the stress-strain curve, up to "a," in Figure 2. As the deformation approaches the transformation region, austenite nucleates heterogeneously at the locations of strain accumulation. By fast formation of austenite phase at the expense of δ-ferrite phase, the strength increases remarkably as austenite takes over deformation.

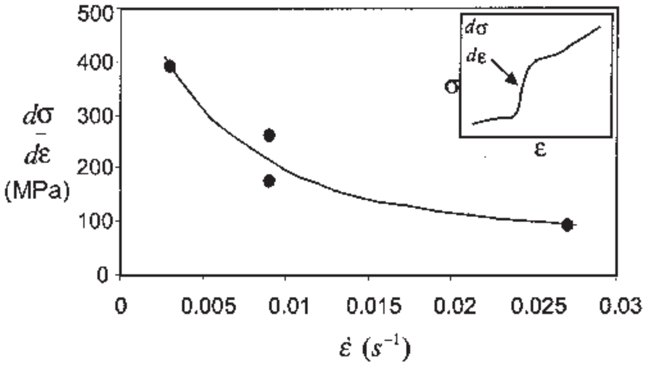

Fig. 9—Effect of strain rate on the linear slope of the $\delta \rightarrow \gamma$ transformation region (Nb steel).

Figure 9 illustrates that this strength transition is strain-rate dependent and takes place more gradually at higher strain rates. At high strain rates, dynamic recovery in δ-ferrite does not catch up with strain hardening as fast as it does at lower strain rates. Therefore, more accumulated strain is stored in δ-ferrite before the "nonequilibrium transformation" region. (The nonequilibrium $\delta \rightarrow \gamma$ transformation is defined as that taking place during the thermal schedule in the absence of any deformation.) This higher internal strain energy can be eliminated through the $\delta \rightarrow \gamma$ transformation, which starts "earlier" or at higher temperatures. Note that such transformation takes place in the metastable transformation region. In this case, the transformation, upon reaching the nonequilibrium region, can proceed by growth of the present austenite grains, since this is more favorable energetically than the nucleation of new grains, which also requires an extra activation energy. However, nucleation of new austenite grains is possible as well. On the other hand, at lower strain rates, the transformation is strain induced at temperatures closer to the nonequilibrium region, where the transformation driving force is also greater. This can lead to a larger number of austenite nuclei in the metastable transformation region. The reason for this is simply because the nucleation activation energy is reduced by the strain energy and smaller austenite embryos can exceed the activation energy barrier of nucleation. Figure 9 shows that the transition of strength takes place more rapidly at lower deformation rates. Since the nonequilibrium transformation occurs within a narrow temperature region (<30 °C) and the cooling rate in the thermal schedules is 10 °C/s, it is reasonable to expect smaller austenite grains when the strain-induced transformation initiates closer to the nonequilibrium region. In other words, the lower the strain rate, the smaller the austenite grain size.

B. *Failure Mode Analysis*

As explained previously in the results section, the failure in both steels is composed of ductile and brittle modes. The brittleness is described as grain boundary decohesion. This is also associated with some limited and localized plastic deformation and, hence, is different from the brittleness at low temperatures where cleavage fracture prevails. Such plastic deformation, which appears as "void formation and coalescence" and "deformation striations" on grain surfaces, is defined as embrittlement, which is manifested as grain boundary separation.

Examination of the microstructure near the fracture region (Figure 10) explicitly shows that grain boundary separation was a result of void formation and coalescence at grain boundaries, mostly at grain boundary triple junctions. It was also noticed that the void formation process was assisted by grain boundary MnS and Al_2O_3 particles, 500 nm to 1 μm in size. As well, Figure 10(b) demonstrates that grains have slid over each other during tension at the straightening stage. The arrows in Figure 10(b) indicate the sliding direction of two adjacent grains. Hence, grain boundary sliding contributed to the fracture. There only remains the explanation for the underlying mechanism for the void formation at grain boundaries.

In polycrystalline materials, the relative deformation between neighboring grains must be accommodated at their common grain boundaries. It has been suggested that grain boundary sliding can be a mechanism for accommodating strain incompatibility between neighboring grains.[19] Moreover, there is a general agreement that more than 50 pct of the total strain in superplastic deformation is proceeded by grain boundary sliding.[20] This implies that grain boundary sliding is basically a deformation mechanism rather than an effective embrittling mechanism leading to fracture at low strains. However, this is true as long as the sliding is accommodated by plastic flow in the grain interior. Otherwise, the accommodation takes place through void and crack formation at the sliding boundaries.

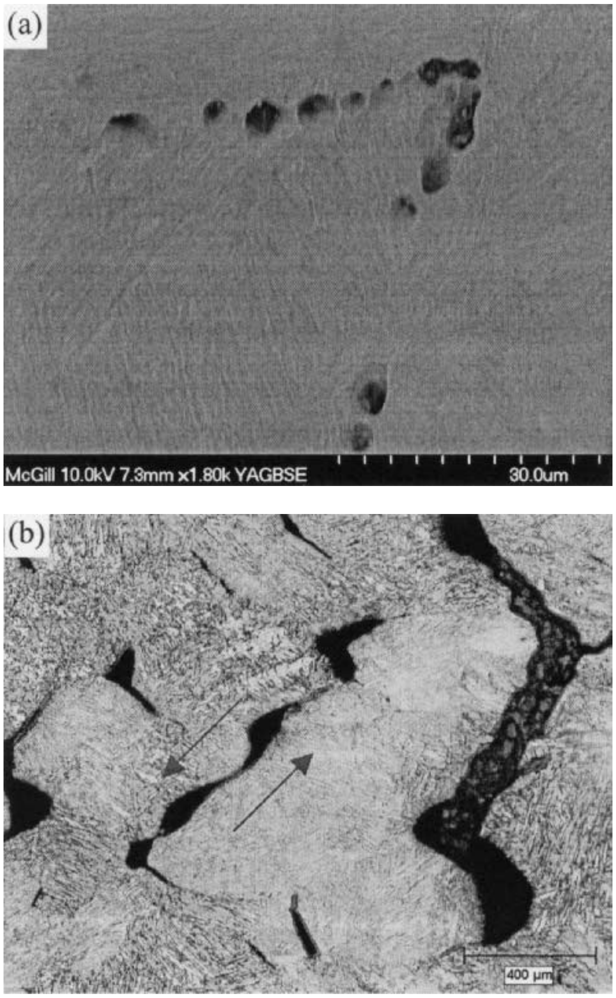

Fig. 10—Longitudinal sections of the Nb steel subjected to the thermal schedule alone. (*a*) Backscattered SEM image explaining void formation at grain boundary triple junction and (*b*) grain boundary sliding (arrows indicate the sliding direction) (etched with picral).

In the Nb-containing steel, Nb atoms can pin dislocations both as a solute and in the form of precipitates. Vacancies, generated during deformation, form vacancy-Nb atom complexes and these complexes diffuse toward and subsequently decompose at dislocation cell walls.[21] Such Nb segregation at dislocations not only imposes a drag effect on dislocations, but also the local supersaturation of Nb enhances Nb(CN) precipitation. Both of these pin dislocations and retard further flow, as well as inhibit dynamic recovery and recrystallization in austenite, especially in as-cast austenite.[1,21,22] Consequently, plastic flow in the lattice is limited and grain boundary sliding has to be accommodated by void nucleation at grain boundaries. Since this is viable in both the Nb steel and the B steel, the occurrence of dynamic recrystallization in the B steel (Figure 8(a)) is most probably related to some interaction between B and Nb atoms. This issue is beyond the scope of this article and will be discussed elsewhere.[23]

Conclusively, the relative resistance of the austenite grain interior to plastic flow determines if austenite grain boundary sliding leads to an early fracture. In other words, the more deformation sustained by the grain interior, the less detrimental the grain boundary sliding.

C. *Mechanism of Hot Ductility Improvement*

As Table II revealed, predeformation during the $\delta \rightarrow \gamma$ transformation led to 6 pct and 26 to 38 pct improvement in the hot ductility of the B steel and the Nb steel, respectively. The limited improvement in the B steel is likely due to its high intrinsic hot ductility when it is subjected to the thermal schedule alone. As Figure 7(a) suggests, this is attributed to a grain refinement mechanism, such as dynamic recrystallization, at the straightening stage. Comparing the Nb-steel microstructures just before the tensile test at the straightening stage (Figure 8(b)) and immediately after the fracture (Figure 8(a)), it appears that recrystallization was underway during the tension. This could have contributed to the hot ductility improvement in the Nb steel, as well. The recrystallized microstructure (Figure 8(a)) displays grain sizes varying from 9.5 to 42 μm with an average of 32 μm. In addition, the grain aspect ratio (length/width) changes from 2.3 to 7.9, whereas it varies from 2.1 to 4.6 in the specimen subjected to the thermal schedule alone (Figure 7(b)). The larger grain aspect ratio in the former indicates that more deformation took place in the grain interior.

Although all three specimens in Figure 3 demonstrated grain refinement after fracture at the straightening stage, the occurrence of dynamic recrystallization is not conclusive since there is no "hump" or stress peak, which is the characteristic of dynamic recrystallization (Figure 3(b)). In fact, even though dynamic recrystallization begins before the stress peak occurs, the presence of stress peaks on constant strain rate flow curves is often considered to be the only indication of the initiation of dynamic recrystallization. Flow curves without well-defined stress peaks, but which display a steady state, are generally believed to pertain to dynamic recovery as the only restoration mechanism. Nevertheless, dynamic recrystallization takes place in many materials even though no clearly defined stress peaks are observed in laboratory flow curves. Examples of such materials include Nb-microalloyed low-carbon and austenitic stainless steels.[24,25]

From a consideration of thermodynamic instability, Poliak and Jonas[26,27,28] established a critical kinetic condition for the initiation of dynamic recrystallization. This condition, which is based on the dislocation strain energy, corresponds to an inflection point on the θ-σ curve, where θ is the strain-hardening rate $\left(\frac{\partial\sigma}{\partial\varepsilon}\right)$ and σ is stress. In other words, dynamic recrystallization starts when $\frac{\partial}{\partial\sigma}\left(\frac{\partial\sigma}{\partial\sigma}\right) = 0$. Gottstein *et al.*[29] recently studied this criterion with regard to microstructural instability in terms of the substructure. Because their predicted results showed good agreement with the criterion proposed by Poliak and Jonas, *i.e.*, the inflection point model, they suggested that one internal parameter is dominant, namely, the one that most strongly affects the flow stress at large strains. In this respect, Gottstein *et al.*'s model approaches the inflection point model, so that, essentially, the flow stress is represented in terms of the total dislocation density.

The inflection point model was recently employed to study dynamic recrystallization in compression experiments.[27,28] Even though it should be also applicable in tension experiments, caution should be exercised when grain boundary decohesion and deformation localization are concerned. This is because such phenomena can affect the flow curve, leading to a strain-hardening behavior that is not solely dependant on dislocation characteristics.

Because load cells generally do not render exact instantaneous values, but reveal very short-range fluctuations around the actual load, as can be seen in Figure 3(b), strain hardening appears iteratively positive and negative, even though it is always positive before the maximum stress is reached. Therefore, in order to study the strain-hardening behavior, the experimental deformation curve must be smoothed; the best approach is to approximate it with a polynomial of appropriate order. This was performed for specimens I through III of Figure 3(b), and the corresponding strain-hardening behaviors are shown in Figure 11. As can be seen in Figure 11(a), the rate of decrease in θ decelerates with an increase in flow stress until the critical stress (σ_c) corresponding to the onset of dynamic recrystallization is reached. At this point, $\frac{\partial}{\partial\sigma}\left(\frac{\partial\theta}{\partial\sigma}\right) = 0$. With increasing strain, θ again starts to decrease rapidly at an increasing rate. This quantity tends to infinity as the flow stress approaches its peak value, σ_p, at $\theta = 0$.

In addition, because $\left(\frac{\partial\theta}{\partial\sigma}\right)_{\dot{\varepsilon}} = \left(\frac{\partial\ln\theta}{\partial\varepsilon}\right)_{\dot{\varepsilon}}$, the ln θ-ε plot must also exhibit an inflection at the onset of dynamic recrystallization. Accordingly, the critical strain for dynamic recrystallization can be determined, as shown in Figure 11(b).

Figure 11 shows that the ratios of σ_c/σ_p and $\varepsilon_c/\varepsilon_p$ remain fairly constant at about 0.78 and 0.48, respectively. These values are consistent with those reported by Poliak and Jonas, being 0.85 and 0.5, respectively, obtained in compression experiments for a Nb steel.[27,28] However, in contrast to compression, σ_p in tension does not necessarily correspond to dynamic recrystallization. There are striking qualitative similarities in the θ-σ behavior associated with dynamic recrystallization and that displayed when flow localization occurs in tension. The onset of dynamic recrystallization and flow localization (necking) are both manifested through the appearance of an inflection point in the θ-σ curve.[26] It was noticed that the θ-σ plot in different specimens of the Nb steel and the B steel, and under conditions that dynamic recrystallization did not take place, exhibited inflections during tension testing to failure.[22] Obviously, these inflections are attributed to flow localization and/or grain boundary decohesion. Under these conditions, it was found that the ratios of σ_c/σ_p and $\varepsilon_c/\varepsilon_p$ were respectively greater than 0.84 and 0.60. Therefore, in tension, an inflection point that is relatively close to the ultimate tensile strength indicates the onset of failure rather than dynamic recrystallization. Tentatively, it appears that, in order to verify the occurrence of dynamic recrystallization in tensile experiments, $\varepsilon_c/\varepsilon_p$ seems to be a reliable measure to begin with; *i.e.*, $\varepsilon_c/\varepsilon_p > 0.6$ is less likely to be attributed to dynamic recrystallization. However, it is difficult to rationalize this observation. Therefore, the occurrence of dynamic recrystallization can only be conclusively confirmed from an analysis of the microstructure.

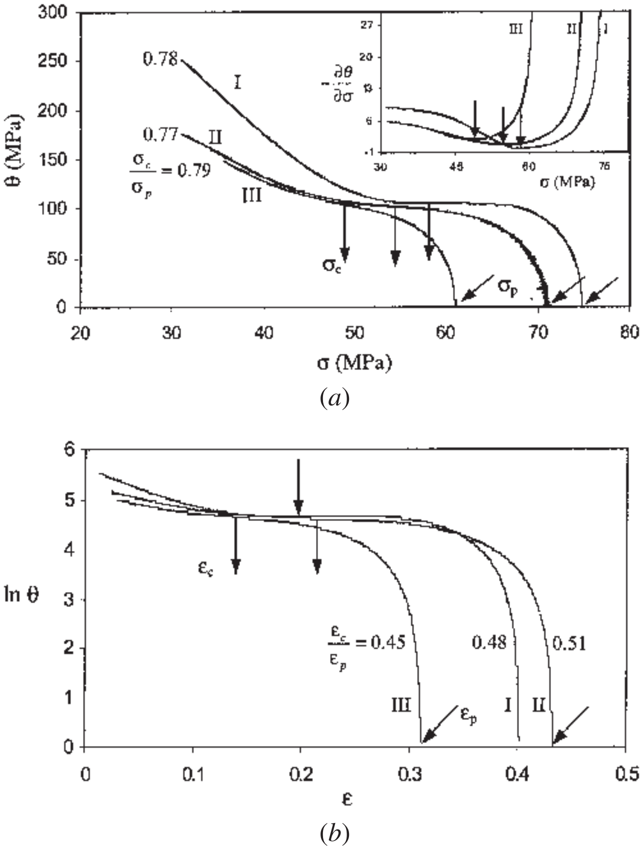

(*a*)

(*b*)

Fig. 11—Strain hardening rate plots *vs* stress and strain for specimens I through III in Fig. 3(b).

Assuming that the peak strains in Figure 11(b) correspond to the dynamic recrystallization, the initial grain sizes can be calculated. It was found that, in a microalloyed steel containing 0.03 wt pct Nb, ε_p behaves as follows;[30]

$$\varepsilon_p = 5.8 \times 10^{-4} d_0^{0.5} \mathrm{Z}^{0.16}$$

where $Z = \dot{\varepsilon} \exp\left(\frac{Q_{\text{def}}}{\mathrm{R}T}\right)$, d_0 is the initial grain size, and Q_{def} is the deformation activation energy, with the other parameters having their usual definitions. Referring to Eq. [4] in Reference 30, which correlates the deformation activation energy and chemical composition, Q_{def} is calculated to be 313.26 kJ/mol for the Nb-steel examined here. This value is very close to that obtained experimentally for a Nb-bearing low-carbon steel (319 kJ/mol) displaying dynamic recrystallization.[27] Using this approach, the initial grain sizes at the straightening stage, before the tensile experiment, are approximated to be 240, 277, and 144 μm in specimens I, II, and III (Figure 3), respectively. The smallest grain size in specimen III, which was subjected to the lowest rate of precompression during the $\delta \rightarrow \gamma$ transformation, corresponds to the fact that it underwent the fastest rate of $\delta \rightarrow \gamma$ transformation (Figure 9). Note that this grain size calculated for specimen III is finer than the actual average grain size observed in Figure 8(b), *i.e.*, ~220 μm. This suggests that the actual recrystallization ε_p is greater than the peak strain specified in Figure 11(b). In other words, the strain to reach the ultimate tensile strength is lower than the dynamic recrystallization peak strain.

Specimen I was expected to have the largest initial grain size because it had been subjected to the highest predeformation rate during the $\delta \rightarrow \gamma$ transformation. It should be noted that all recrystallization models have been constructed from the results obtained from reheated specimens that can have different microstructural characteristics, *e.g.*, grain size, precipitate, and segregation, than those developed after melting and solidification. For instance, under a given experimental condition, the temperature for dynamic recrystallization can be higher in the as-cast structure.[22] The effect of the as-cast structure on dynamic recrystallization characteristics is a subject that needs to be further investigated.

From these results, it can be concluded that the occurrence of dynamic recrystallization at the straightening stage is the reason for the improvement of hot ductility in the Nb steel. During recrystallization, grain boundaries migrate and microvoids initially formed at grain boundaries are isolated from the boundaries. Consequently, the coalescence of microvoids at grain boundaries is prevented and grain boundary decohesion is retarded. Dynamic recrystallization at the straightening stage is initiated because of the austenite grain refinement during the precompression in the vicinity of the $\delta \rightarrow \gamma$ transformation (Figure 8(b)). Such grain refinement could have occurred either by the accelerated $\delta \rightarrow \gamma$ transformation or through static/dynamic recrystallization of austenite after completion of the $\delta \rightarrow \gamma$ transformation. Or, during precompression, both mechanisms contributed to grain refinement; *i.e.*, dynamic transformation led to grain refinement, which in turn led to recrystallization in austenite. This is explained in the following paragraph.

Considering the RA values in Table II and comparing specimens I and II in Figure 4, which were respectively predeformed in the δ-ferrite region and the $\delta \rightarrow \gamma$ transformation region, there is an improvement in the hot ductility from 13 to 27 pct when predeformation goes through the transformation region. In addition, no further improvement occurred after an increase in predeformation to $\varepsilon = 0.08$, *i.e.*, specimen IV in Figure 4. Hence, it appears that 13 pct (the difference between 28 and 15 pct), as compared to the effect of the thermal schedule alone (Table II), is the maximum improvement attainable solely by the accelerated $\delta \rightarrow \gamma$ transformation. This is ascribed to a smaller austenite grain size resulting from the strain-induced transformation. On the other hand, predeformation after the $\delta \rightarrow \gamma$ transformation resulted in only 8 pct (the difference between 23 and 15 pct) improvement in the hot ductility (specimen V in Figure 4). Such an improvement can only be attributed to the elimination of solidification shrinkages by precompression, since no grain refinement was observed in the microstructure. Then, the sum of improvements due to the predeformations during and after the $\delta \rightarrow \gamma$ transformation is 21 pct (8 pct + 13 pct), provided these two predeformation schedules have been applied separately to two different specimens. This is less than the minimum 26 pct (the difference between 41 and 15 pct, Table II) improvement in the hot ductility after the application of 0.1 continuous predeformation, initiated before and continued after the transformation (specimen III in Figure 3). Therefore, since the grain size in specimen IV of Figure 4, *i.e.*, ~350 μm, is larger than the grain size in specimen III of Figure 3, *i.e.*, 220 μm, there appears to have been a recrystallization after the transformation in the latter. In other words, the smaller austenite grain size resulted from the accelerated transformation was further refined by the subsequent recrystallization. Even though dynamic recrystallization has played the major role in the second stage of the grain refinement process, the possible contribution of metadynamic/static recrystallization cannot be ruled out, especially since the temperature was high enough to overcome the activation energy in the given time frame. The very small grains in Figure 8(b) can be ascribed to this phenomenon.

V. CONCLUSIONS

1. The deformation-induced $\delta \rightarrow \gamma$ transformation is strain-rate dependent. The higher the strain rate, the more gradual the transformation. This can be attributed to the kinetics of transformation, which is mainly controlled either by nucleation or by growth.
2. It was recognized that grain boundary sliding is the mechanism of failure at the straightening stage in the as-cast Nb-microalloyed steel.
3. Addition of B to the Nb-containing steel is beneficial to the hot ductility. This is due to the occurrence of dynamic recrystallization, which isolates grain boundary cavities. Therefore, void coalescence is suppressed and grain boundary separation is retarded.
4. Application of deformation in the vicinity of the $\delta \rightarrow \gamma$ transformation refines the subsequent austenite grains. Hence, dynamic recrystallization is encouraged at the straightening stage and the hot ductility is improved considerably.

ACKNOWLEDGMENTS

The authors gratefully acknowledge the financial support from the Canadian Steel Research Association and the Natural Science and Engineering Research Council of Canada.

REFERENCES

1. B. Mintz, S. Yue, and J.J. Jonas: *Int. Mater. Rev.*, 1991, vol. 36 (5), pp. 187-217.
2. T.H. Coleman and J.R. Wilcox: *Mater. Sci. Technol.*, 1985, vol. 11 (1), pp. 80-83.
3. J.K. Brimacombe and K. Sorimachi: *Metall. Trans. B*, 1977, vol. 8B, pp. 489-505.
4. P. Sricharoenchai, C. Nagasaki, and J. Kihara: *Iron Steel Inst. Jpn. Int.*, 1992, vol. 32 (10), pp. 1102-09.
5. Y. Maehara, K. Yasamoto, H. Tomono, T. Nagamichi, and Y. Ohmori: *Mater. Sci. Technol.*, 1990, vol. 6, pp. 793-806.
6. W.T. Lankford: *Metall. Trans.*, 1979, vol. 3, pp. 1331-57.
7. E. Hurtado-Delgado and R.D. Morales: *Metall. Mater. Trans. B*, 2001, vol. 32B, pp. 919-27.
8. G.I.S.L. Cardoso, B. Mintz, and S. Yue: *Ironmaking Steelmaking (UK)*, 1995, vol. 22 (5), pp. 365-77.
9. B. Mintz, J.M. Stewart, and D.N. Growther: *Trans. Iron Steel Inst. Jpn.*, 1987, vol. 27 (12), pp. 959-64.
10. B. Mintz: *Iron Steel Inst. Jpn. Int.*, 1999, vol. 39 (9), pp. 833-55.
11. F. Zarandi and S. Yue: *Proc. Materials Science and Technology Conf.*, ISS, Warrendale, PA, 2003, pp. 21-31.
12. N.E. Hannerz: *Trans. Iron Steel Inst. Jpn.*, 1985, vol. 25 (2), pp. 149-58.
13. S.K. Kim, J.S. Kim, and N.J. Kim: *Metall. Mater. Trans. A*, 2002, vol. 33A, pp. 701-04.
14. X.L. He, M. Djahazi, J.J. Jonas, and J. Jackman: *Acta Metall. Mater.*, 1991, vol. 39 (10), pp. 2295-308.
15. M. Jahazi and J.J. Jonas: *Mater. Sci. Eng. A*, 2002, vol. 335 (1–2), pp. 49-61.
16. A.M. Elwazri: Master's Thesis, McGill University, Montreal, 1998.
17. S. Akhlaghi: Ph.D. Thesis, McGill University, Montreal, 2000.
18. H.J. Frost and M.F. Ashby: *Deformation-Mechanism Maps*, Pergamon Press, New York, 1982.
19. Y. Zhang, J. Ma, X. Li, and C. Cao: *Mater. Sci. Forum*, 1994, vols. 170–172, pp. 495-500.
20. B.P. Kashyap, A. Arieli, and A.K. Mukherjee: *J. Mater. Sci.*, 1985, vol. 20 (8), pp. 2661-86.
21. W.J. Liu: *Metall. Mater. Trans. A*, 1995, vol. 26A, pp. 1641-57.
22. F. Zarandi: Ph.D. Thesis, McGill University, Montreal, 2004.
23. F. Zarandi and S. Yue: McGill University, Montreal, Canada, unpublished research, 2004.
24. N.D. Ryan and H.J. McQueen: *Can. Metall. Q.*, 1990, vol. 29 (2), pp. 147-62.
25. S.H. Cho, K.B. Kang, and J.J. Jonas: *Iron Steel Inst. Jpn. Int.*, 2001, vol. 41 (1), pp. 63-69.
26. E.I. Poliak and J.J. Jonas: *Acta Mater.*, 1996, vol. 44 (1), pp. 127-36.
27. E.I. Poliak and J.J. Jonas: *Iron Steel Inst. Jpn. Int.*, 2003, vol. 43 (5), pp. 684-91.
28. J.J. Jonas and E.I Poliak: *Mater. Sci. Forum*, 2003, vols. 426–432, pp. 57-66.
29. G. Gottstein, M. Frommert, M. Goerdeler, and M. Zeng: *Z. Metallkd.*, 2003, vol. 94 (5), pp. 628-35.
30. S.H. Cho, K.B. Kang, and J.J. Jonas: *Iron Steel Inst. Jpn. Int.*, 2001, vol. 41 (7), pp. 766-73.